AeroBest 2021
Lisboa, 21-23 July 2021


# MODELING AND OPTIMIZATION OF AN OBSTACLE DETECTION SYSTEM FOR SMALL FIXED-WING UAV

**N. M. P. Alturas** * **and A. C. Marta**

IDMEC
Instituto Superior Técnico
Universidade de Lisboa
Av. Rovisco Pais 1, 1049-001 Lisboa, Portugal
{nuno.alturas,andre.marta}@tecnico.ulisboa.pt, https://www.idmec.tecnico.ulisboa.pt/

**Abstract.** *A solution for the enhancement of safety during the flight of small fixed-wing UAVs, regarding the detection of obstacles during flight, is presented. This was achieved by making a market study on available sensors to find the most suitable to equip a UAV and by modeling them, so that these models could be integrated into collision detection and avoidance simulations. Different tracking filters and sensor fusion techniques were studied, where the Converted Measurement Kalman Filter and the Weighted Filter technique were found to be the best to implement. In the simulations, the Potential Fields avoidance method was chosen for being computationally inexpensive and for providing feasible solutions in real time. Several parametric studies were conducted to test the performance of the selected sensors and to assess how their different parameters affect the success of the obstacle avoidance. An optimization study was also conducted, using a global optimizer, to find the orientation of sensors, for different sets of sensors, that results in the best performance for a set of randomly generated collision scenarios with both stationary and moving obstacles. Relatively simple detection configurations were found that still provide high collision avoidance success rate.*

**Keywords:** Potential Fields, Genetic Algorithm, Kalman Filter, Unbiased Conversion, Sensor Fusion

## 1 INTRODUCTION

Like many other technologies, Unmanned Aircraft Vehicles (UAVs) were initially developed for military purposes and have since made their way into the civil domain. Nowadays, UAV applications include, but are not limited to, photography and video, precision agriculture, inspections, monitoring and deliveries. The market continues to grow and projections show that non-military UAV production will total 14.3 billion dollars in 2028, while totaling 4.9 billion dollars in 2019 [1].

UAV classification is important to differentiate existing systems, since each category has different legal regulations, and also commercial and operational purposes. Considering the classification of UAVs [2], our work is specifically aimed at fixed-wing mini UAVs (maximum take-off weight $< 25$ kg, range $< 10$ km, endurance $< 2$h and flight altitude $< 120$ m), which accounts for the majority of the market share for their versatility and low-cost, but lack efficient and robust safety systems. A representative example of such UAV category is the Tekever AR4 shown in Fig.1, that has a maximum take-off weight of 4 kg, an endurance of 2 hours and a maximum speed of 15 m/s [3].

Figure 1: Tekever AR4 UAV [3].

For the UAVs to perform the missions previously described efficiently, autonomous and Beyond Visual Line of Sight (BVLOS) flight is essential, which is already foreseen by the European law. To that end, for a safe flight to be possible, a robust and reliable Obstacle Sense and Collision Avoidance (S&A) system is needed.

There are already numerous proposals for avoidance algorithms and sensor layouts, but most are limited to multi-rotor UAVs. Adapting these systems to fixed-wing UAV characteristics and keeping the cost low continues to be a challenge. Among the many vision based applications [4], obstacle detection has been developed significantly. The hardware solutions range from simple monocular cameras, either to complement GPS data [5] or even in GPS deprived environments [6]. Better performance is obtained using binocular vision [7] or RGB-D cameras (with depth sensor) [8] at an expense of higher on-board computational power. Much simpler solutions have been proposed with low cost ultrasonic and infrared range finders, but they are limited to low-speed and high-maneuverability multi-rotor UAVs due to their limited sensing range [9]. Advanced solutions often include sensor fusion, where data is gathered from multiple sources. There are many possible combinations of sensors but some representative examples include merging monocular cameras with RADAR [10], and ADS-B with a thermal camera [11]. It should be noted that the latter poses significant limitations since it cannot detect non-ADS-B-equipped aircraft under adverse meteorological conditions.

Therefore, the main goal of this work is to improve the safety of low-cost fixed-wing mini UAVs regarding the detection of obstacles during their flight. It is part of an extensive two-stage sense and avoidance system, being focused on the former.

## 2 SENSORS BENCHMARK

A thorough study was conducted on the various types of sensors available on the market that could be integrated into our representative UAV. After this analysis, one sensor of each type was picked to be compared in terms of range and field of view (FOV), so that their attributes and flaws could be better showcased. The chosen sensors for this comparison were the uAvionix pingRX ADS-B [12], the Lightware LW20/C laser rangefinder [13], the Aerotenna $\mu$Sharp Patch RADAR [14], the Intel D435 stereo camera [15] and the MaxBotix MB1242 sonar [16]. Their corresponding sensed areas on the horizontal plane are represented in Fig.2, except for the ADS-B sensor since it is omnidirectional and its range depends on the power of the other aircraft emitted signal. The sonar FOV is almost invisible as a result of its small range (two orders of magnitude below the RADAR range).

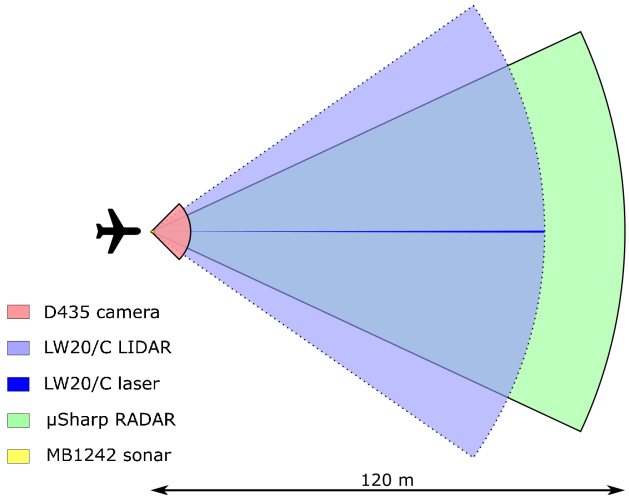


Figure 2: Comparison of several sensor ranges and FOVs.

It is important to note that the LIDAR is based on the laser rangefinder, being its multidirectionality obtained from coupling a scanning actuator. In Fig.2, an arbitrary but typical 70° horizontal FOV was chosen and, because of this, the limits of the sensed area were dotted. The LW20/C's laser area, when the scanning mode is not activated, is represented in dark blue, where its 0.3°beam divergence can be observed.

The camera sensed area is associated with its depth image sensors. The infra-red and color cameras have their own range and FOV but these are more applicable to complement other sensors as they do not provide depth data.

Based on this comparison, the ultrasound and stereo vision sensors were not modeled in Sec. 3 due to their very limited range, as identifying obstacles when they are only at a distance of 10 m or 0.765 m generally do not result in successful avoidance maneuvers when the UAV is traveling at a maximum cruise speed of 15 m/s. The ADS-B was also excluded for being a cooperative sensor, meaning it would require other vehicles to be equipped with similar equipment to allow the UAV to detect them, which is outside the scope of this work.

## 3 SENSORS MODELS

A sensor model is an abstraction of the actual sensing process that describes the information a sensor can provide, how this information is limited by the environment and how it can be enhanced by data obtained from other sensors.

For the developed simulations, different sensors were modeled to compare their behavior and find the combination that produce the best S&A results. The sensors are characterized by their range, FOV, accuracy and data acquisition frequency. The values used for these parameters are from the sensors presented in Sec. 2, which were obtained from their technical manuals or inferred from available data, and are summarized in Tab.1. Since our simulations were restricted to the horizontal plane of motion, the vertical FOV is not relevant.

Table 1: Characteristics of the different sensors used in simulations.

| | Laser rangefinder | LIDAR | RADAR |
|---|---|---|---|
| Range (m) | 100 | 100 | 120 |
| Horizontal FOV (°) | 0.3 | variable | 50 |
| Accuracy (m) | 0.2 | 0.2 | 0.22 |
| Max. frequency (Hz) | 388 | 388 | 90 |

### 3.1 LIDAR/Laser Rangefinder

Fayad and Cherfaoui [17] presented an approach to solve the problem of tracking partially hidden objects by a single layer laser scanner to be used in driving situations. In their proposed method, if an object is totally visible, it is considered that its half was detected and the remaining of the obstacle is reconstructed assuming symmetry, where the center of symmetry is the medium point of the segment connecting the first and last point of the cluster. In our simulations, the obstacles were modeled as circles, so this distance corresponds to the diameter of the obstacle.

That same reference [17] also provides a solution to the errors caused by the higher distance between consecutive points in farther obstacles which results in smaller detected dimensions, as seen in Fig.3, where the modeled obstacle is considerably smaller than the real obstacle. To solve this problem, the measured diameter is passed through the time

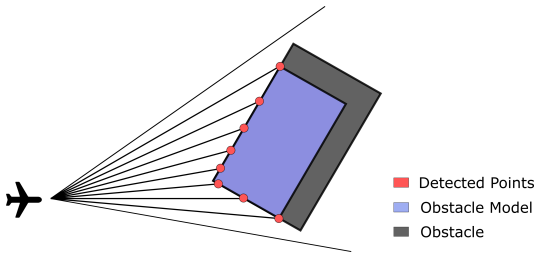


Figure 3: Obstacle reconstruction using a LIDAR.

filter

$$D_k = D_{k-1} + G(D_{meas} - D_{k-1})\,, \tag{1}$$

where $G$ $(0 < G < 1)$ is the filter gain, $D_k$ is the filtered diameter at instant $t_k$, $D_{k-1}$

is the filtered diameter at instant $t_{k-1}$, and $D_{meas}$ is the measured dimension at instant $t_k$. The gain needs to be carefully selected as it impacts the speed of the variation of the dimensions. A small gain corresponds to a slow variation and it is preferable for noisy environments but not suitable for high relative speed objects. The gain can be determined by

$$G = 1 - \sqrt[n]{1-p}\,, \tag{2}$$

where $p$ corresponds to a fraction that represents the desired accuracy of the dimensions and $n$ corresponds to the number of filter cycles required to get an accuracy of $p$.

Regarding the tracking phase, classical Kalman filters [18] were used, where the motion of detected obstacles is considered to be two-dimensional, linear and constant between consecutive scans. This simplification describes the state of the targets with an acceptable error, considering a high scanning frequency. This model assumes a LIDAR that only scans horizontally, but if the rangefinder was to be attached to a gimbal with two degrees of freedom, it would have to be extended to include the third dimension.

### 3.2 RADAR

To evaluate the system performance, the RADAR sensor was modeled in the context of the Sense and Avoid system. So, this model addresses the angular accuracy, update rate, range and FOV, rather than being a lower-level model that would deal with signal and environment modeling.

Assuming the RADAR sensor outputs the range, bearing and elevation of the detected obstacles, the state estimation becomes more complex than the estimation used in the LIDAR model, as these outputs are polar whereas the intruder dynamics are best expressed in rectangular coordinates. The chosen RADAR model was the converted measurement Kalman filter (CMKF) due to its simple implementation [19]. The following equations reflect a 2-D model, as used in the simulations presented, but it can easily be extended to 3-D.

The unbiased conversion [20] was used, as the standard conversion method gives biased inconsistent estimates for certain levels of cross-range measurement error owing to the nonlinear transformation of the noisy bearing. Using the unbiased conversion, modeling the measurement errors as Gaussian white noise, the compensation of the bias is multiplicative and the conversion is given by

$$x_m^u = \lambda_\alpha^{-1} r_m \cos(\alpha_m) \tag{3}$$

$$y_m^u = \lambda_\alpha^{-1} r_m \sin(\alpha_m)\,, \tag{4}$$

where ($x_m^u$,$y_m^u$) are the measurements converted to the Cartesian frame, $r_m$ is the measured range, $\alpha_m$ is the measured azimuth and $\lambda_\alpha$ is the bias compensation factor expressed as

$$\lambda_\alpha = e^{-\sigma_\alpha^2/2}\,, \tag{5}$$

where $\sigma_\alpha$ is the standard deviation of the noise in the azimuth measurements.

The covariance matrix used in the Kalman Filter is given by

$$\mathbf{R}_u = \begin{bmatrix} var(x_m^u|r_m,\alpha_m) & cov(x_m^u, y_m^u|r_m,\alpha_m) \\ cov(x_m^u, y_m^u|r_m,\alpha_m) & var(y_m^u|r_m,\alpha_m) \end{bmatrix}\,, \tag{6}$$

with the details of the computation of these variances found in reference [20].

## 4 MULTISENSOR DATA FUSION

When the sensing system is composed of multiple sensors, the input data provided by the sensors needs to be merged in some way. In this work, the weighted filter method [21] was used.

A weight is evaluated for each sensor, which is related to its reliability. The UAV needs to be equipped with reference data sensors, which provide information about the UAV state. IMUs and optical flow sensors are examples of reference data sensors used to evaluate the reliability of the main sensor data and help to decide between those sensors, based on the rationale that changes in distance to obstacles correspond to analogous changes in the UAV position. If the obstacles are stationary, then these variations should coincide. If the obstacles are moving, that information becomes corrupted, but it is unlikely that that motion corresponds better to randomly wrong measurements. The weights are then computed by comparing all possible sensor combinations of main data and reference data using a differential norm.

The obstacle distance measurement corresponding to the sensor with the lowest weight is selected in the current time instance of the sensing process, while the remaining are rejected based on the idea that they are corrupted. However, if the computed weights have a low variation, the sensor values are fused according to their weights.

## 5 OBSTACLE DETECTION AND AVOIDANCE ALGORITHMS

The collision detection and avoidance algorithm used in the subsequent simulations is based on the work developed in reference [22]. Each detected obstacle has several safety zones associated with it, which play a role in the obstacle detection phase as well as in the collision avoidance phase.

The obstacles were modeled as circles and, as such, the collision radius ($R_c$) defines the occurrence of collision if it is trespassed. The safety radius ($R_s$) defines the minimum distance that should be maintained between the UAV and the obstacle to take into account possible deviations and uncertainties that could happen during the detection and path prediction phases. The action radius ($R_a$) is the distance from which the replanned paths begins to depart from the original path given by the global planner. Lastly, the detection radius ($R_d$) represents the distance from which an obstacle is considered by this algorithm. The $R_s$ should be similar to the UAV size; the $R_a$ should be comparable to the $R_s$ and the $R_d$ corresponds to the range of the sensors used. A representation of the described safety zones is displayed in Fig.4.

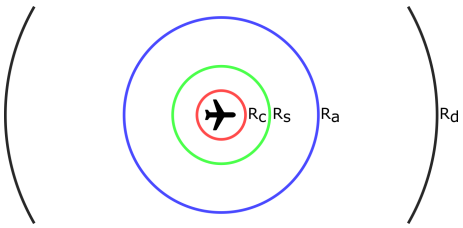


Figure 4: Representation of the safety zones around an obstacle.

### 5.1 Geometric Collision Detection Method

The chosen collision detection method computes straight projections of the obstacles, considering future distances between the obstacles and the UAV [23]. As such, the resulting collision detection method consists of computing the closest point of approach (CPA) between the UAV and the target, assuming that both will maintain constant velocities and rectilinear paths. If the CPA distance is smaller than the safety radius $R_s$, an evasive maneuver must be performed, otherwise the obstacle is not considered a threat to the UAV.

In case of multiple collisions being detected, the obstacles are sorted by their time for collision $t_{CPA}$, so that the obstacles associated with possible earlier collisions are avoided first.

### 5.2 Potential Fields Method

To solve the local path planning problem, the Potential Fields approach is used, where the waypoints and obstacles are considered charged particles [24]. Considering this analogy, the waypoints generate an attractive field, the obstacles a repulsive field and the sum of all forces is used to generate the direction of motion.

The attractive potential is given by

$$\mathbf{f}_{at} = \alpha_{PF} \frac{P_c - P}{||P_c - P||} + (1 - \alpha_{PF}) \frac{P_n - P_c}{||P_n - P_c||}, \tag{7}$$

where the first term is responsible for guiding the UAV to the nearest point of the global path and the second term is responsible for guiding the UAV to the next defined waypoint. $P$ is the the UAV position, $P_c$ is the closest point of the global path and $P_n$ is the position of the next waypoint. The parameter $\alpha_{PF}$ is responsible for giving more or less predominance to each term. An example of a global path to a waypoint and its corresponding attractive potential field is represented in Fig.5 for $\alpha_{PF} = 0.7$.

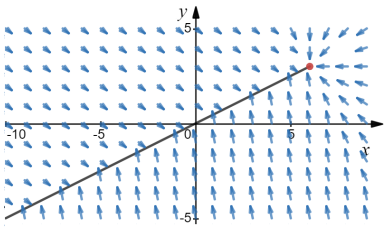


Figure 5: Attractive field for a linear path.

Using a simple repulsive potential to avoid obstacles is not feasible since that would lead to irregular motion around the obstacle. Instead, the potential associated to the obstacle is described by

$$\mathbf{f}_{rep} = \begin{cases} \infty \frac{\mathbf{d}_0}{||\mathbf{d}_0||} & \text{if } ||\mathbf{d}_0|| \leq R_c \\ S_m \mathbf{s} & \text{if } R_c < ||\mathbf{d}_0|| \leq R_s \\ S_m \frac{R_a - ||\mathbf{d}_0||}{R_a - R_s} \mathbf{s} & \text{if } R_s < ||\mathbf{d}_0|| \leq R_a \\ 0 & \text{if } ||\mathbf{d}_0|| \geq R_a \vee \theta \leq \theta_c \end{cases}. \tag{8}$$

This way, the field is different according to the distance between the obstacle and the UAV. If the UAV is in the collision zone, the field will be repulsive ($\mathbf{d}_0$ is the vector

pointing from the obstacle to the UAV) with infinite intensity. If it is in the safety zone, the field will have the direction of **s**, a swirling term that makes the UAV maneuver in the correct direction, and the intensity of $S_m$, a constant to be defined depending on the velocity of the UAV. In the action zone, the field is similar to the previous one but with the addition of a gradient term that ensures the intensity of the field decreases linearly with the distance of the UAV to the obstacle until becoming null for $||\mathbf{d}_0|| = R_a$. Lastly, outside the action zone, the obstacle has no influence in the motion of the UAV, thus the field intensity is null. To avoid the UAV being trapped around the obstacle, the generated field needs to become zero once the obstacle is overcome. To achieve this, the angle $\theta$ between the desired direction of motion and the direction of the obstacle is also computed and the field becomes null if $\theta$ is smaller than a defined cut-off angle $\theta_c$. A potential field associated with an obstacle is displayed in Fig.6 for $R_c = 2$, $R_s = 3$ and $R_a = 6$.

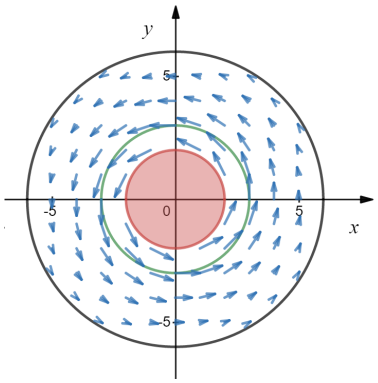


Figure 6: Repulsive field for an obstacle.

## 6 UAV MODEL DEFINITION

Since the S&A simulations were performed in a two-dimensional environment, the most important performance parameters to define are the UAV speed (V) and the maximum yaw rate that defines the angular velocity ($\omega$) of its turns. Considering the Tekever AR4 described in Sec.1, the UAV speed considered varied between 8 m/s and 15 m/s. The faster it moves, the larger its yaw rate capability needs to be so that the obstacles can be effectively avoided. To prove this concept, a series of simulations were performed where the UAV was set in a head-on collision course with a moving obstacle with a 2 m radius and a safety radius of 2 m that moves with opposite velocity of the UAV. The UAV was equipped with a RADAR with 50° FOV and 120 m range. For each speed, the maximum yaw rate was decreased until the UAV could not perform the avoidance maneuver without breaching the safety zone $R_s$. The results are presented in Fig.7, where a linear dependency can be recognized.

To check the roll angles corresponding to the speeds and yaw rates obtained, the avoidance maneuver is approximated to a coordinate turn [25], where the turning is made at a constant vertical angular velocity with null lateral force. Considering no wind, the sideslip angle is almost null and the angle of attack and climb angle are very small, being the speed and angular velocity related by $tan(\phi) = \frac{\omega V}{g}$, where $\phi$ is the roll angle and $g$ is the gravitational acceleration. Some of the obtained values are displayed in Tab.2. The roll angles obtained are acceptable considering the urgency of the maneuvers needed to

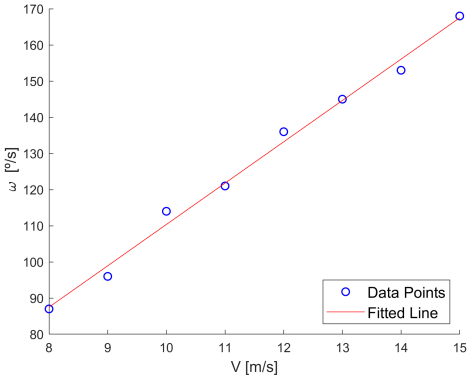


Figure 7: Minimum yaw rate capability to avoid obstacle safely for different speeds.

Table 2: Roll angles for each maneuver considering a coordinate turn.

| V (m/s) | Yaw rate (°/s) | Roll Angle (°) |
|---|---|---|
| 8 | 87 | 51.1 |
| 10 | 114 | 63.8 |
| 12 | 136 | 71.0 |
| 15 | 168 | 77.4 |

avoid obstacles. Since, for the highest speed of 15 m/s, the corresponding roll angle is high but achievable nonetheless, the maximum UAV yaw rate was set to 168°/s for the subsequent simulations.

As described in Sec. 3, using polar measurements and a Cartesian state space leads to inaccuracies when tracking the obstacles with a Kalman filter. To test the measurement error covariance matrix described in that section, the UAV was put in a head-on collision course, where the UAV is moving at 8 m/s and the obstacle is moving at 10 m/s. The UAV was equipped with a RADAR with the specifications of the Aerotenna $\mu$Sharp Patch (100 m range, 50° FOV and 0.22 m accuracy). The noise was divided into a radial and an angular component, where both components were modeled as a zero-mean Gaussian noise, with the corresponding variance chosen so that 99.73% of the set would be within the accuracy range. The angular accuracy was considered at half the sensor range (50 m). To perform this test, one hundred simulations were performed for the unbiased conversion matrix, the standard conversion matrix and the identity matrix (as a control group), then, the average position errors were computed for both Cartesian coordinates. The root mean square (RMS) deviation for the three matrices for both spatial coordinates is listed in Tab.3. Only the first 250 scans were considered in the computations, so that the points where the obstacle is not detected anymore do not influence this metric, as the avoidance maneuver starts after this point. From Tab.3, one can conclude that using the standard conversion or the unbiased conversion result in very similar results. This may be due to the particular conditions of our study, where the sensor range and the noise variance are not very high. Despite the similar results, the unbiased conversion matrix was selected for all subsequent simulations.

Table 3: Root mean square deviations for each of the used matrices.

| RMS (m) | $x$ axis | $y$ axis |
|---|---|---|
| Standard conversion matrix | 0.0165 | 0.0013 |
| Unbiased conversion matrix | 0.0163 | 0.0016 |
| Identity matrix | 0.5993 | 0.0009 |

## 7 SENSOR PARAMETRIC STUDIES

The response of the UAV to imminent collisions, when equipped with sensors with different parameters, is studied to verify whether the chosen sensors perform acceptably.

To study how the sensor range influences the response of the UAV to detected obstacles, the UAV was set in a head-on collision course with an obstacle animated with an incoming speed of 10 m/s with a radius of 2 m and a safety radius of 4 m. The UAV is traveling at 8 m/s and it is equipped with a RADAR sensor pointing forward with 50° FOV, though the type of sensor does not affect the results significantly. In Fig.8, the different collision avoidance trajectories with varying sensor ranges are presented. The obstacle

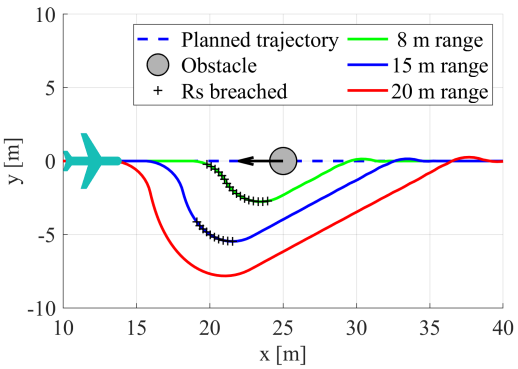


Figure 8: Avoidance trajectories for different RADAR ranges for head-on collision threat.

is always properly tracked and avoided, which results in similar tight maneuvers. If the UAV is equipped with a RADAR with a range of 8 m, it is already inside the action radius of the obstacle when the obstacle is detected. Then, it immediately initiates the avoidance maneuver but cannot avoid breaching the safety radius of the obstacle. For this particular scenario, sensing ranges greater than 20 m result in identical collision avoidance trajectories.

To test the effect of the FOV of the sensor on the avoidance capabilities of the UAV, the UAV was set in a 60° angled collision course with an obstacle moving at a speed of 12 m/s, while being equipped with a LIDAR that performs a measurement every half degree with a range of 100 m. The LIDAR gain from Eq.(2) also needs to be defined. For the sensor to reach 99% of the real dimensions, $p$ is set to 0.99 and, to get this precision before the obstacle transverses 10% of the 100 m range, the filter needs to perform 20 iterations ($n$), considering the LIDAR is working at a 50 Hz frequency and assuming the obstacles can move at the same speed of the UAV, which results in a maximum relative speed of 30 m/s. Knowing $n$ and $p$, the minimum gain to be used can be computed using

said equation, it being 0.2057. The responses of the UAV for different FOVs, when it is moving at a speed of 8 m/s, is displayed in Fig.9. For FOVs greater than 66°, the obstacle

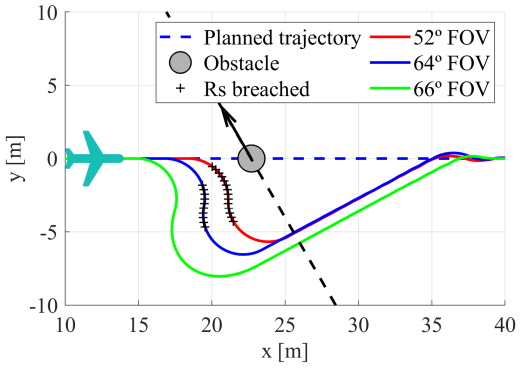


Figure 9: Avoidance trajectories for different LIDAR FOVs for angled collision threat.

is properly tracked in advance, which results in a proper safe maneuver. For a FOV of 52°, the obstacle is detected when it is already dangerously close to the UAV so the UAV breaches the safety radius for several points, despite avoiding a collision. Finally, for smaller FOVs, the UAV cannot avoid the collision because the available actuation time is simply too short for the evasion maneuver to be executed. This also covers the case of a fixed laser rangefinder (0° FOV) as the UAV detects the obstacle only when it is directly in front of it, which causes a quick breach of the safety radius. Because of the singular nature of this case, the obstacle velocity can only be tracked with a radial component and so, the obstacle is tracked as being in a head-on collision course with a small velocity.

The obstacles were avoided by the UAVs with different sensors, but the success of the maneuver depends on the approach angle of the obstacle.

Another important parameter studied, but not shown due to its length, was the approximation (relative) velocity between the UAV and the obstacle. As expected, to guarantee the S&A success, the required sensor range and/or FOV needs to be increased as the UAV speed increases, so that the detection occurs earlier, allowing an evasion time that is still smaller than the sensed collision time.

## 8 OPTIMAL SENSING SYSTEM

A study was made to determine the optimal sensor configuration, for four different sensor sets. To that end, fifty collision-leading scenarios were randomly generated, where the UAV speed randomly varied in the range [8,15] m/s and the obstacle parameters were randomly picked from Tab.4. Three examples of such scenarios can be seen in Fig.10.

Table 4: Data for randomly generated imminent collision scenarios.

| # fixed obst. | # moving obst. | obst.radius | obst.speed | obst.direction |
|---|---|---|---|---|
| {0,1,2} | {0,1,2} | [0.5, 2] m | [5, 15] m/s | [0, 90] ° |

Then, a function $f(\beta)$, to be minimized dependent on the sensor orientation $\beta$ was

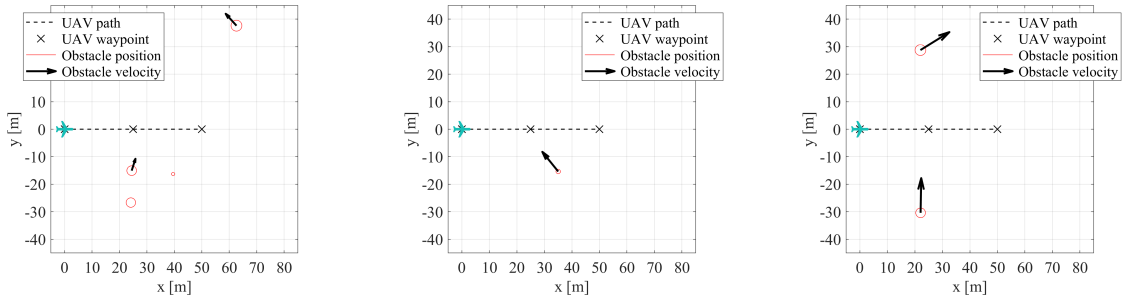


(a) Scenario #2 (b) Scenario #17 (c) Scenario #49

Figure 10: Examples of randomly generated collision-leading scenarios.

defined as

$$f(\beta) = \sum_j \sum_i \left( -d_{min}(i) + \phi_1 |\max(R_s(i) - d_{min}(i), 0)|^2 + \phi_2 |\max(R_c(i) - d_{min}(i), 0)|^2 \right) , \tag{9}$$

where the first term drives the evasion maneuver to maximize the minimum distance $d_{min}$ between the UAV and the obstacle $i$, the second term represents the penalty when the minimum distance violates the safety radius $R_s$ ($d_{min} \leq R_s$), and the last term represents the penalty when the minimum distance violates the obstacle collision radius $R_c$ ($d_{min} \leq R_c$). The metric accumulates not only for every obstacle $i$ in each scenario but also for all scenarios $j$. The weights used were $\phi_1 = 10$ and $\phi_2 = 50$ to penalize more the collision cases than the close-call cases.

The metric defined in Eq.(9) is multi-modal and relatively noisy, as illustrated in Fig.11 for the particular sensor solution case using a pair of laser rangefinders with a 100 m range, symmetrically pointing forward with an angle $\beta$ with respect to the UAV longitudinal axis.

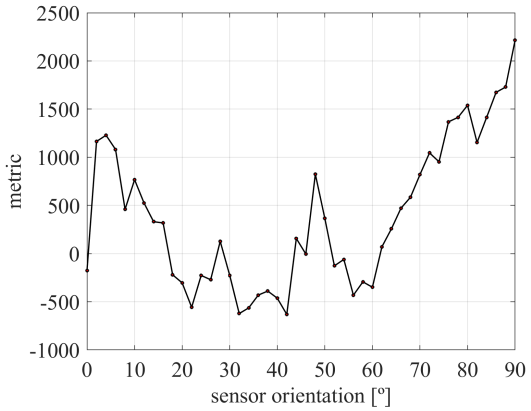


Figure 11: S&A metric as function of sensor orientation.

Given the identified nature of the S&A metric function, the Genetic Algorithm (GA) [26] was used to find its minimum. This is a gradient-free, population-based method, which, instead of working with a single solution candidate, deals with a set of solutions that are updated simultaneously from iteration to iteration, which increases the likelihood

of finding the global optimum. The problem was posed in standard form as

$$\begin{aligned} \text{Minimize} \quad & f(\beta) \\ \text{w.r.t.} \quad & \beta \\ \text{subject to} \quad & \beta_{min} < \beta < \beta_{max} \,, \end{aligned} \tag{10}$$

where $\beta_{min}$ and $\beta_{max}$ are the lower and upper bounds of $\beta$, respectively, to be defined for each particular case.

Before performing the simulations, several optimization parameters needed to be defined: the initial population was set to be created with a uniform distribution; the crossover function was set to create 80% of the population in each generation; because the variables are bounded, the mutation function randomly generates directions that are adaptive with respect to the last successful or unsuccessful generation, where the chosen direction and step length satisfy the set bounds. The convergence criteria were set such that the global minimum was found in a timely but accurate manner: a function convergence of $10^{-3}$ was used with 10 stall generations, and a maximum of 50 generations prescribed. The population size was set to 30 individuals. These parameters were chosen following best practices [27].

### 8.1 Two Laser Rangefinder Solution

For a set of two laser sensors, the orientation of each sensor was bounded between 0° and 70° from the longitudinal axis, in the horizontal plane and, to simplify the problem, the two lasers were considered to have a symmetrical orientation, resulting in just one design variable. A sensing range of 100 m was adopted.

The GA optimization algorithm terminated after 18 generations due to average change in the fitness value less than the specified tolerance, corresponding to 536 function evaluations. The optimal sensor orientation was 39.3°, which corresponds well with one of the approximate minimum shown in the preliminary study in Fig.11. The optimal two laser rangefinder sensor configuration is illustrated Fig.12.

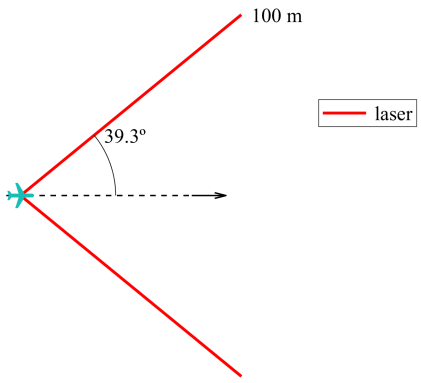


Figure 12: Optimal orientation for two laser rangefinder configuration.

A comparison of performance between the optimal orientation and a single laser pointing forward is presented in Tab.5, where a failure corresponds to a collision with an obstacle and a close call happens if the UAV breaches the safety radius of an obstacle. The optimal configuration results in just two collisions in all 50 scenarios. However, in

52% of the scenarios, the safety radius of obstacles was breached because a UAV equipped only with two laser rangefinders is not capable of properly tracking the moving obstacles when collisions are imminent. Even though the optimal solution holds the same success

Table 5: Performance comparison for different orientations of two laser rangefinders.

| Orientation | Metric | Failure | Close call | Success rate |
|---|---|---|---|---|
| 0° | -176.5 | 2/50 | 36/50 | 96% |
| 39.3° | -958.2 | 2/50 | 26/50 | 96% |

rate (96%) as when only one laser rangefinder pointing forward is used, there is a considerable decrease of close calls, meaning that the likelihood of collisions in a real-scenario is significantly reduced. This is expected as more obstacles approaching from an angle can be detected ahead of the collision.

### 8.2 Two RADAR Solution

Like in the previous study, the two RADAR sensors were considered to be symmetrical about the UAV longitudinal axis, so that only one variable needed to be optimized. Given the previous findings, the orientation variable range was set between 0° and 70°. Each RADAR had a range of 120 m, an accuracy of 0.22 m and a FOV of 20°.

The expected result of this simulation would be a sensor orientation close to 10°, which would yield the same result as if the UAV were equipped with a single RADAR with double (40°) FOV. The optimizer halted after 14 generations due to average change in the fitness value less than the specified tolerance, corresponding to 424 function evaluations. The optimal RADAR orientation was 29.6°, as illustrated in Fig.13.

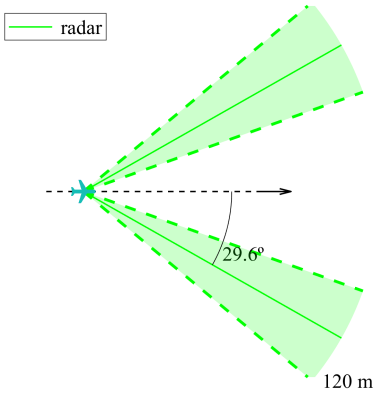


Figure 13: Optimal orientation for two RADAR configuration.

Table 6 compares the performance between the optimal orientation, a 10° orientation and a single RADAR pointing forward. Some failures that occur when the UAV is equipped with one RADAR pointing forward do not happen for the optimal solution because the obstacles that approached the UAV from a steep angle could now be detected, whereas they were undetectable by a single pointing forward RADAR solution.

The optimal solution did not have overlapping FOVs, which would increase the accuracy of the measurements through the data fusion algorithm. Given the set of scenarios

Table 6: Performance comparison for different orientations of two RADARs.

| Orientation | Metric | Failure | Close call | Success rate |
|---|---|---|---|---|
| 0° | 2117.4 | 12/50 | 22/50 | 76% |
| 10° | 810.2 | 10/50 | 15/50 | 80% |
| 29.6° | 257.4 | 8/50 | 15/50 | 84% |

used, having a wider effective FOV revealed to be a more favorable solution than the juxtapositioning, that would correspond to an orientation of 10°.

Compared to the previous case of laser sensors, these simulations demonstrated that the smaller accuracy of RADARs have a high impact on the obstacle tracking precision. Despite their wider FOV, this led to worse overall performance in terms of collisions but better performance in terms of close calls. It is fair to state that the RADAR accuracy is the more important parameter for precise collision avoidance but the RADAR FOV is more important for obstacle detection.

### 8.3 Two Laser Rangefinder and one RADAR Solution

This case involved three sensors: two laser rangefinders symmetrical about the UAV longitudinal axis, whose orientations were bonded between 0° and 70°; and one fixed RADAR pointing forward. Each sensor type had the same characteristics as the ones simulated in the previous two cases.

The optimizer converged in 11 generations, after 340 function evaluations. The optimal laser orientation was 38.3°, as illustrated in Fig.14. Again, the obtained optimal solution did not involve overlapping sensors.

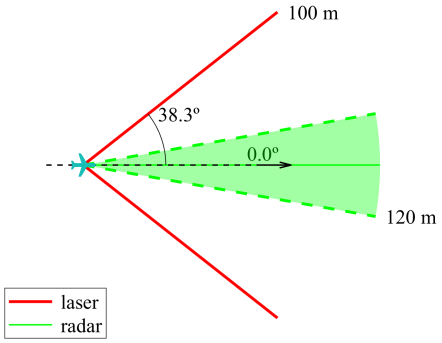


Figure 14: Optimal orientation for two laser rangefinder and one RADAR configuration.

In Tab.7, the optimal solution is compared in terms of S&A performance to the solutions that would result from a UAV being equipped with only one type of sensor, it being two symmetrical laser rangefinders with an orientation of 38.3° or a RADAR pointing forward.

Comparing the performance of each type of sensors separately, the pointing forward RADAR, perhaps due to its narrow FOV (20°), performed much poorly, with as many as 24% collisions, whereas the two lasers pointing sideways (@ 38.3% orientation) led to 8% collisions.

Table 7: Performance comparison for optimal solutions using two lasers and one RADAR.

| Sensors | Metric | Failure | Close call | Success rate |
|---|---|---|---|---|
| 2 lasers @ 38.3° | -163.2 | 4/50 | 27/50 | 92% |
| 1 RADAR @ 0° | 2117.4 | 12/50 | 22/50 | 76% |
| 2 lasers + 1 RADAR | -954.1 | 2/50 | 19/50 | 96% |

As expected, it was the combined 2 lasers + 1 RADAR configuration that held considerably the best results, proving that multiple sensors are required to properly detect not only head-on but also angled approaching obstacles. Using this combination led to just 4% collisions and also the lowest instances of closed calls to obstacles.

### 8.4 Two RADAR and one Laser Rangefinder Solution

The last case consisted of two RADARs symmetrical about the UAV longitudinal axis and one fixed laser rangefinder pointing forward, under the same previous assumptions.

Coincidentally, this case converged in the same iterations as the previous case (11 generations with 340 function evaluations) The optimal RADAR orientation was 30.5°, as illustrated in Fig.15, which meant no sensor overlapping.

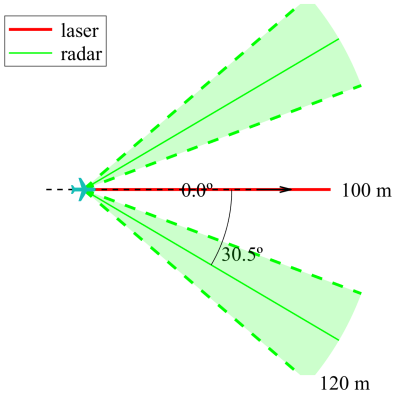


Figure 15: Optimal orientation for two RADARs and one laser rangefinder configuration.

Similarly to the previous case, the optimal solution is compared to the solutions of a UAV equipped with only one type of sensor, as summarized in Tab.8.

Table 8: Performance comparison for optimal solutions using two RADARs and one laser.

| Sensors | Metric | Failure | Close call | Success rate |
|---|---|---|---|---|
| 2 RADARs @ 30.5° | 314.8 | 8/50 | 17/50 | 84% |
| 1 laser @ 0° | -176.5 | 2/50 | 36/50 | 96% |
| 2 RADARs + 1 laser | -1719.3 | 2/50 | 14/50 | 96% |

Analyzing each type of sensors separately, the pointing forward laser led the fewer collisions but considerable more close calls compared to the two RADARs pointing 30.5% sideways. It was the combination of 2 RADARs + 1 laser that led to both lower failure and fewer close calls, due to the improved capability for obstacle detection.

### 8.5 Performance Comparison of the Different Sensor Sets

The performance of the four sensor configurations studied in this work, at optimal orientations, are summarized in Tab.9.

Table 9: Comparison of the optimal performance for the four different sensor sets studied.

| Sensors | Metric | Failure | Close call | Success rate |
|---|---|---|---|---|
| 2 lasers @ 39.3° | -958.2 | 2/50 | 26/50 | 96% |
| 2 lasers @ 38.3°+ 1 RADAR @ 0° | -954.1 | 2/50 | 19/50 | 96% |
| 2 RADARs @ 29.6° | 257.4 | 8/50 | 15/50 | 84% |
| 2 RADARs @ 30.5°+ 1 laser @ 0° | -1719.3 | 2/50 | 14/50 | 96% |

For the set of scenarios tested, the laser rangefinder demonstrated better performance than the RADAR if only one sensor type is to be used. However, this is tightly dependent on the sensor characteristics, such as range, FOV and accuracy.

Among the four configurations tested, it was the two RADAR and 1 laser rangefinder that not only produced the least collisions but also led to the least close calls. Unexpectedly, the combination of different type of sensors revealed more advantageous. From these findings, it is expected that increasing even more the number of sensors would lead to even better performance, thought at a higher hardware cost.

## 9 CONCLUSIONS

This work focused on the first stage of the S&A phase, responsible for the acquisition of the necessary information that allows the vehicle to detect threatening situations. Our goal was to study simple, and yet effective, safety enhancing obstacle detection solutions for fixed-wing mini UAVs.

A selection of sensors in terms of range, FOV, accuracy and cost, led to the conclusion that laser/LIDARs and RADARs are the most adequate to this particular application, in detriment of ultrasound, and stereo vision and ADS-B sensors. Simulation models were developed for each of the relevant sensors, that were then integrated into an avoidance system. For laser rangefinders and LIDARs, classic Kalman filters were sufficient to guarantee adequate tracking, but for the RADARs, a Converted Measurement Kalman Filter with unbiased conversion was required. At a decision level, the weighted filter technique was selected for the data fusion from different redundant sensors due to its simplicity and effectiveness.

Having modeled the sensors, several parametric studies were made, where the impact of the range and field of view of the vehicle in the avoidance of obstacles from predetermined scenarios was made clear. From these simulations, the specifications of the studied sensors were verified as more than acceptable for avoiding obstacles at the considered speed range.

Additionally, some optimization studies were conducted to determine the best orientation of the sensors on the UAV for different sets of sensors. The optimization process was accomplished by using a genetic algorithm to minimize a metric related to the minimum distance to the obstacles, with penalties in case of safety radius breach and collisions. It is clear that the required range depends on the relative speed towards the obstacles. Provided that the sensor ranges are sufficiently large, their FOV becomes the most relevant parameter so that the UAV surroundings can be properly scanned for obstacles.

Overall, the developed sensor configurations provided very satisfactory performance for obstacle detection for fixed-wing mini UAVs in the simulated environment.

The best sensor configuration will always depend on the UAV performance and the minimum acceptable obstacle S&A success rate. UAVs with high maneuverability or low speeds do not require very advanced sensing systems but if the allowed S&A failure rate is to be kept very low, then the opposite is holds.

Future work includes the study of other possible combination of sensors and the implementation and validation of the simulated optimal solutions in both terrestrial and aerial test vehicles.

## REFERENCES

[1] P. Finnegan. *2019 World Civil Unmanned Aerial Systems Market Profile & Forecast*. Teal Group Corporation, Aug. 2019.

[2] K. Dalamagkidis. Classification of UAVs. In K. P. Valavanis and G. J. Vachtsevanos, editors, *Handbook of Unmanned Aerial Vehicles*, pages 83–91. Springer Netherlands, 2015. doi:10.1007/978-90-481-9707-1_94.

[3] TEKEVER AR4. `http://uas.tekever.com/ar4-evo//`. Accessed: 24-11-2020.

[4] C. Kanellakis and G. Nikolakopoulos. Survey on computer vision for uavs: Current developments and trends. *J Intell Robot Syst*, 87:141—168, 2017. doi:10.1007/s10846-017-0483-z.

[5] L. Jian and L. Xiao-min. Vision-based navigation and obstacle detection for uav. In *2011 International Conference on Electronics, Communications and Control (ICECC)*, pages 1771–1774, 2011. doi:10.1109/ICECC.2011.6066586.

[6] S. Saha, A. Natraj, and S. Waharte. A real-time monocular vision-based frontal obstacle detection and avoidance for low cost uavs in gps denied environment. In *2014 IEEE International Conference on Aerospace Electronics and Remote Sensing Technology*, pages 189–195, 2014. doi:10.1109/ICARES.2014.7024382.

[7] Z. Chen, X. Luo, and B. Dai. Design of obstacle avoidance system for micro-uav based on binocular vision. In *2017 International Conference on Industrial Informatics - Computing Technology, Intelligent Technology, Industrial Information Integration (ICIICII)*, pages 67–70, 2017. doi:10.1109/ICIICII.2017.87.

[8] M. Odelga, P. Stegagno, and H. H. Bülthoff. Obstacle detection, tracking and avoidance for a teleoperated uav. In *2016 IEEE International Conference on Robotics and Automation (ICRA)*, pages 2984–2990, 2016. doi:10.1109/ICRA.2016.7487464.

[9] N. Gageik, P. Benz, and S. Montenegro. Obstacle detection and collision avoidance for a UAV with complementary low-cost sensors. *IEEE Access*, 3:599–609, 2015. doi:10.1109/ACCESS.2015.2432455.

[10] H. Yu, F. Zhang, P. Huang, C. Wang, and L. Yuanhao. Autonomous obstacle avoidance for uav based on fusion of radar and monocular camera. In *2020 IEEE/RSJ International Conference on Intelligent Robots and Systems (IROS)*, pages 5954–5961, 2020. doi:10.1109/IROS45743.2020.9341432.

[11] A. Carrio, Y. Lin, S. Saripalli, and P. Campoy. Obstacle detection system for small uavs using ads-b and thermal imaging. *J Intell Robot Syst*, 88:583—595, 2017. doi:10.1007/s10846-017-0529-2.

[12] *PING-RX ADS-B Dual Receiver*. uAvionix, 2019.

[13] *LW20 / SF20 LiDAR sensor Product manual*. Lightware, 2018. Rev 9.

[14] *μSharp Patch Collision Avoidance Radar*. Aerotenna, 2018.

[15] *Intel RealSenseTM D400 Series (DS5) Product Family*. Intel, 2018. Rev 001.

[16] *MB1242 Datasheet*. MaxBotix, 2012.

[17] F. Fayad and V. Cherfaoui. Tracking objects using a laser scanner in driving situation based on modeling target shape. In *2007 IEEE Intelligent Vehicles Symposium*, pages 44–49, June 2007. doi:10.1109/IVS.2007.4290089.

[18] M. S. Grewal, A. P. Andrews, and C. G. Bartone. Kalman filtering. pages 355–417. Wiley Telecom, 2020.

[19] D. Lerro and Y. Bar-Shalom. Tracking with debiased consistent converted measurements versus EKF. *IEEE Transactions on Aerospace and Electronic Systems*, 29(3): 1015–1022, July 1993. doi:10.1109/7.220948.

[20] M. Longbin, S. Xiaoquan, Z. Yiyu, S. Z. Kang, and Y. Bar-Shalom. Unbiased converted measurements for tracking. *IEEE Transactions on Aerospace and Electronic Systems*, 34(3):1023–1027, 1998. doi:10.1109/7.705921.

[21] N. Gageik, P. Benz, and S. Montenegro. Obstacle detection and collision avoidance for a UAV with complementary low-cost sensors. *IEEE Access*, 3:599–609, May 2015. doi:10.1109/ACCESS.2015.2432455.

[22] J. Alves. Path planning and collision avoidance algorithms for small RPAS. Master's thesis, Instituto Superior Técnico, June 2017.

[23] B. Albaker and N. Rahim. Unmanned aircraft collision detection and resolution: Concept and survey. In *5th IEEE Conference on Industrial Electronics and Applications*, pages 248–253, June 2010. doi:10.1109/ICIEA.2010.5516808.

[24] A. Alexopoulos, A. Kandil, P. Orzechowski, and E. Badreddin. A comparative study of collision avoidance techniques for unmanned aerial vehicles. In *2013 IEEE International Conference on Systems, Man, and Cybernetics*, page 1969–1974, Oct. 2013. doi:10.1109/SMC.2013.338.

[25] B. Etkin and L. D. Reid. *Dynamics of flight*, volume 2. Wiley New York, $3^{rd}$ edition, 1959.

[26] M. J. Kochenderfer and T. A. Wheeler. *Algorithms for Optimization*. MIT Press, 2019. ISBN 9780262039420.

[27] Mathworks ®. Global optimization toolbox ™: User's guide (r2020b). `https://www.mathworks.com/help/pdf_doc/gads/gads.pdf`, 2020. Accessed: 29-12-2020.